nature structural & molecular biology

Structural characterization of full-length NSF and 20S particles

Lei-Fu Chang[1,2,5], Song Chen[1,2,5], Cui-Cui Liu[1,2,5], Xijiang Pan[1,2], Jiansen Jiang[1,2,4], Xiao-Chen Bai[1,2], Xin Xie[1,2], Hong-Wei Wang[2,3] & Sen-Fang Sui[1,2]

The 20S particle, which is composed of the *N*-ethylmaleimide–sensitive factor (NSF), soluble NSF attachment proteins (SNAPs) and the SNAP receptor (SNARE) complex, has an essential role in intracellular vesicle fusion events. Using single-particle cryo-EM and negative stain EM, we reconstructed four related three-dimensional structures: Chinese hamster NSF hexamer in the ATPγS, ADP-AlFx and ADP states, and the 20S particle. These structures reveal a parallel arrangement between the D1 and D2 domains of the hexameric NSF and characterize the nucleotide-dependent conformational changes in NSF. The structure of the 20S particle shows that it holds the SNARE complex at two interaction interfaces around the C terminus and N-terminal half of the SNARE complex, respectively. These findings provide insight into the molecular mechanism underlying disassembly of the SNARE complex by NSF.

In eukaryotic cells, membrane trafficking requires the evolutionarily conserved SNARE proteins[1,2], which consist of v-SNARE on vesicle membranes and t-SNARE on target membranes[3]. During membrane fusion, SNARE proteins on opposing membranes coil together to form a highly stable four-helix bundle[4–6]. The SNARE complex is believed to be the minimum machinery necessary to drive membrane fusion[7]. After membrane fusion, SNARE complexes must be disassembled into individual SNARE proteins for reuse, and NSF and its adaptor protein, SNAP, are responsible for the disassembly process[8,9]. A functional complex consisting of NSF, SNAP and the SNARE complex, termed the 20S particle, was previously discovered and purified by sedimentation[10]. NSF disassociates the SNARE complex upon ATP hydrolysis, making the proteins available for recycling. The mechanism of how the stable SNARE complex is disassembled, however, is still unknown.

NSF belongs to the ATPases associated with various cellular activities (AAA+) family, which is found in all life kingdoms[11,12]. AAA+ proteins are involved in a range of cellular processes, such as protein degradation and DNA replication in all organisms, and membrane fusion and movement of microtubule motors in eukaryotes. Similarly to many other AAA+ proteins, NSF functions as a homohexamer[13], each subunit consisting of three domains: the N-terminal domain (N, 1–205) and two AAA+ domains (D1, 206–477, and D2, 478–744)[14,15]. The N domain is essential for interaction with the α-SNAP–SNARE complex, whereas the D1 domain provides the main ATPase activity required for SNARE disassembly, and the D2 domain promotes nucleotide-dependent hexamerization[16].

Crystal structures of the hexameric D2 domain[17,18] and the N domain[19–21] of NSF have been solved for over a decade, but crystal structures of the D1 domain and the full-length NSF are still not available. Electron microscopic analysis has provided the rough structural layout for each element of the 20S particle[22–24], but claims regarding the overall arrangement of NSF and p97 have been inconsistent. NSF and p97 share considerable sequence similarity and have comparable domain organizations. However, it has been proposed that they adopt different hexameric structures, with the characteristic D1 and D2 domains arranged as an antiparallel structure in NSF, as demonstrated by a cryo-EM map[24], versus a parallel structure in p97, as seen in its crystal structure[25,26]. Additionally, despite the availability of crystal structures making up many parts of the 20S particle, including the SNARE complex[4–6], the yeast homolog of α-SNAP, Sec17 (ref. 27), and some portions of the NSF, there is no three-dimensional structure for the entire 20S particle. These issues restrict our mechanistic understanding of the role of the NSF in disassembling the SNARE complex.

In this study, we used electron microscopy and single-particle analysis to reconstruct the structures of Chinese hamster ovarian NSF in each of its three nucleotide states (ATPγS, ADP-AlFx and ADP) and in the 20S particle. The structures demonstrate a parallel arrangement between the D1 and D2 domains, suggest how nucleotides control the activation of NSF, and how a force may be generated in NSF through ATP hydrolysis, and reveal how the SNARE complex is anchored in the 20S particle. These findings provide important insight into the disassembly process of the SNARE complex by NSF.

[1]State Key Laboratory of Biomembrane and Membrane Biotechnology, Tsinghua University, Beijing, China. [2]Center for Structural Biology, School of Life Sciences, Tsinghua University, Beijing, China. [3]Tsinghua-Peking Center for Life Sciences, Tsinghua University, Beijing, China. [4]Present address: Department of Microbiology, Immunology and Molecular Genetics, University of California, Los Angeles, Los Angeles, California, USA. [5]These authors contributed equally to this work. Correspondence should be addressed to S.-F.S. (suisf@mail.tsinghua.edu.cn).

Received 21 August 2011; accepted 20 December 2011; published online 5 February 2012; doi:10.1038/nsmb.2237

RESULTS

Reconstitution of functional NSF in homogeneous states

One obstacle hindering the reconstruction of NSF at high resolution is its conformational heterogeneity, which has been reported in previous NSF studies[24]. We reasoned that it is probably due to the heterogeneous nucleotide states of each NSF protomer within a hexamer. To overcome this problem, we reconstituted NSF hexamers from monomers in the apo state. NSF monomers were obtained by incubating purified NSF with apyrase and eluted from a size-exclusion chromatography column consistent with the expected molecular weight of 80 kDa. Monomers showed an A_{260nm}/A_{280nm} ratio of 0.674 compared to 0.907 for the NSF hexamer in buffer without nucleotide (**Fig. 1a**), indicating that bound nucleotides had been extensively removed. Monomers in the apo state were then incubated for six hours in the presence of corresponding nucleotides, followed by gel filtration purification to obtain hexamers in homogeneous ATPγS (a nonhydrolyzable analog of ATP), ADP-AlFx (ATP hydrolysis transition state analog) and ADP states. In order to verify that the reconstituted NSF hexamers are functional in their active states, we carried out *in vitro* disassembling assays of SNARE complexes by NSF and α-SNAP in the presence of ATP and Mg^{2+} (**Fig. 1b** and **Supplementary Fig. 1a**,**b**). Indeed, all three reconstituted NSF species under different nucleotide states could still exchange their nucleotides for the free ATP in solution and could disassemble the SNARE complex substrates, as shown by the representative experiment using NSF hexamer reconstituted in the ADP state (**Fig. 1b**) (data for the other two states are not shown). As controls, SNARE complex alone, SNARE complex incubated with α-SNAP, or SNARE complex incubated with α-SNAP and NSF without Mg^{2+} (ATP-EDTA) was not disassembled.

NSF structures visualized by negative stain EM

We first studied the structures of NSF in the ATPγS, ADP-AlFx and ADP states by negative stain EM (**Supplementary Fig. 1c**). The 2D average images from the classification of particles show the typical top, side and oblique views of each state (**Fig. 1c**), demonstrating that NSF has a three-layered structure with a wheel-like top view in the ATPγS and ADP-AlFx states but a two-layered structure with a rosette-shaped top view in the ADP state (**Supplementary Fig. 1d**). The bottom layers are similar to the corresponding projections of the crystal structure of the D2 hexamer, suggesting that the bottom layer is the D2 domain, the middle layer is the D1 domain and the top layer is the N domain (**Fig. 1c**,**d**). The N domain assignments were confirmed by comparison with the class averages of D1-D2 (the N domain truncation mutant of NSF, **Fig. 1e**). The topology of the molecule was further verified by cryo-EM reconstructions and docking analysis of D2 and D1 domains (see below). The apparent six-fold symmetry in the central portion of the top-view class averages of each state is consistent with a hexameric structure of the protein. The unevenly distributed periphery densities in the top-view class averages of NSF

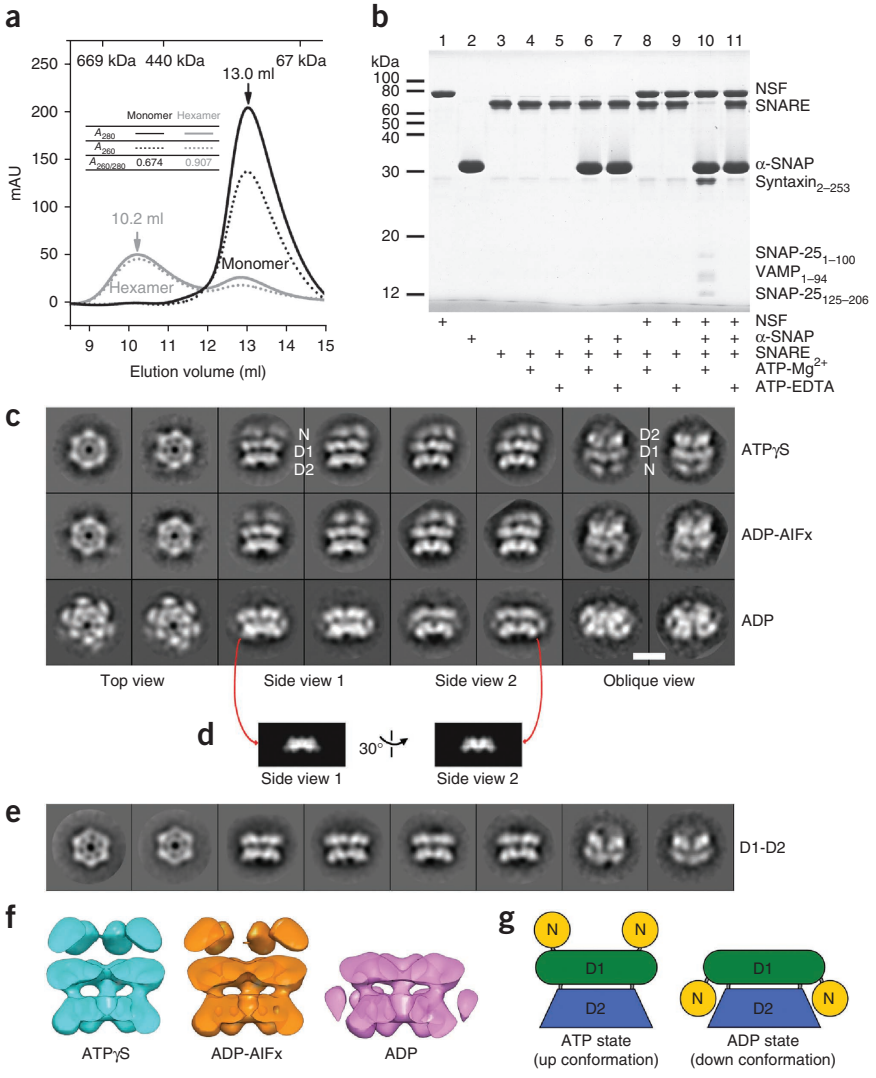

Figure 1 Sample preparation and negative stain EM of NSF in different nucleotide states. (**a**) Purification of NSF monomer and hexamer by size-exclusion chromatography in buffer with no nucleotide. The A_{260nm} and A_{280nm} traces and their ratio for the monomer and hexamer are shown. mAU, milliabsorbance units. (**b**) Disassembly of the SNARE complex by NSF *in vitro*. The SNARE complex was disassembled by reconstituted NSF (in the ADP state) and α-SNAP in the presence of ATP and Mg^{2+} (lane 10). Samples were analyzed by SDS-PAGE without boiling, and gels were stained with Coomassie blue. (**c**) Representative 2D class averages of NSF hexamer in the three different states, ATPγS, ADP-AlFx and ADP. No symmetry was imposed during classification. Four typical classes (top view, two side views and an oblique view) are shown in each state for comparison. Scale bars, 10 nm. (**d**) Two projections of the NSF D2 hexamer map, transformed from the D2 hexamer crystal structure (PDB 1NSF) at a resolution of 16 Å, are shown. The corresponding values in the class averages of EM are indicated by red lines. (**e**) Typical classes of the N domain truncation mutant of NSF, D1-D2. (**f**) The 3D reconstructions of the NSF hexamer in the ATPγS (cyan), ADP-AlFx (orange) and ADP (purple) states. Cut-open side views are shown. (**g**) Schematic presentations of NSF in the ATP state (ATPγS and ADP-AlFx states in the reconstructions) and ADP state. The N, D1 and D2 domains are in yellow, green and blue, respectively. The N domain undergoes a large movement from up conformation to down conformation.

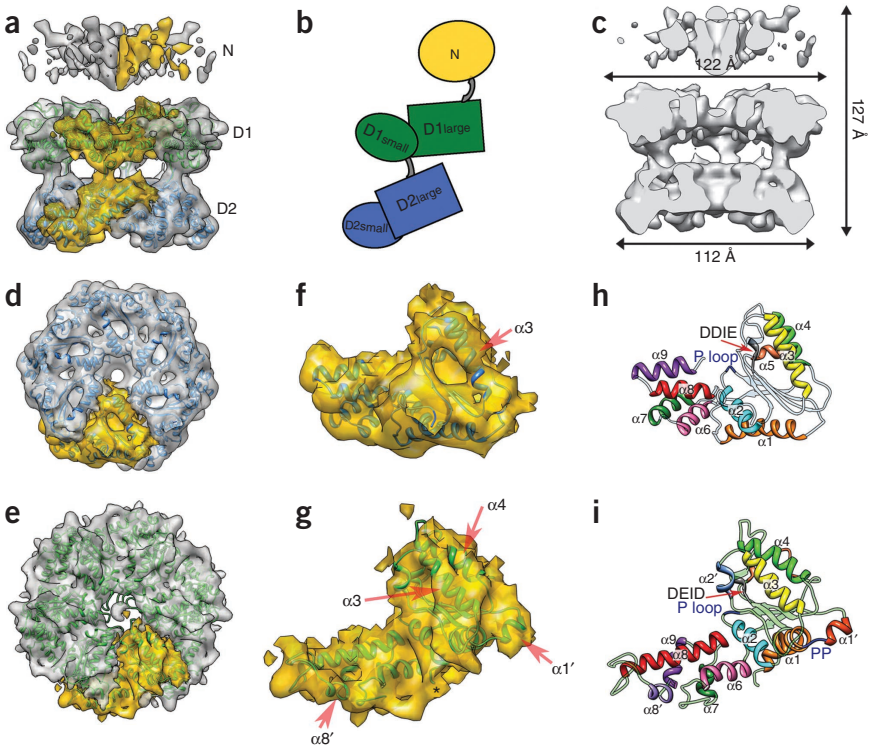

Figure 2 Cryo-EM structure of NSF in the ADP-AlFx state. (**a**) The 3D reconstruction of NSF in the ADP-AlFx state at 9.2-Å resolution with the crystal structure docked (D2 in blue, D1 in green). The D2 hexamer crystal structure (PDB 1NSF) and D1 structure modeled from p97 D1 hexamer crystal structure (PDB 3HU2) were used for flexible fitting in all the structures shown. The N domain was flexible and showed a smaller volume than expected, so we could not dock the crystal structure of NSF-N onto the density map. One protomer is highlighted in gold. (**b**) A schematic presentation of a protomer in NSF hexamer in ADP-AlFx state showing the relationship of the large and small subdomains within D1 and D2. (**c**) Cut-open side view of the 3D reconstruction of NSF in the ADP-AlFx state. (**d**,**e**) Top views of the D2 and D1 hexamer maps isolated from the 3D reconstruction of NSF, as shown in **a**. One protomer is highlighted in gold. (**f**,**g**) Zoomed-in top views of D2 and D1 protomers isolated from **d** and **e**, respectively. Discernible helices are indicated with red arrows. The black star (*) indicates the N terminus of D1. (**h**) Flexibly fitted D2 protomer as in **f**. Nine α-helices, the P-loop and the DEXX box (DDIE) of the AAA module are labeled according to the D2 crystal structure[17]. (**i**) Flexibly fitted D1 protomer as in **g**. Helices α1–9 are labeled according to D2, and the excess helices are labeled as α1′, α2′ and α8′, because they follow α1, α2 and α8. The P loop and the DEXX box (DEID) of the AAA module are indicated.

in the ADP state indicate the flexibility of this portion, which probably corresponds to the N domain (see below).

Based on the negative stain EM data, we reconstructed 3D structures of NSF in the three nucleotide states at a resolution of ~18 Å, with six-fold symmetry imposed (**Fig. 1f** and **Supplementary Fig. 1e**,**f**). These reconstructions suggest a pattern of nucleotide-dependent movement of the N domains (**Fig. 1g**). In the ATP state (ATPγS and ADP-AlFx states in the experiments), the N domains are located on the top of D1, whereas in the ADP state, they move preferentially to the periphery, between D2 and D1 (**Supplementary Fig. 1d**). This pattern is different from the previously reported conformation of NSF obtained by quick-freeze–deep-etch electron microscopy[22]. We refer to the conformation of N domains on the top as the 'up' conformation and that in the periphery as the 'down' conformation (**Fig. 1g**). Because the NSF in the ATPγS and ADP-AlFx states share a similar EM structure, the most apparent conformational change of NSF during its ATPase cycle occurs after γ-phosphate release, specifically, between the ADP-AlFx and ADP states. Thus, we further investigated the structures of NSF in the ADP-AlFx and ADP states under frozen-hydrated conditions to compare the differences between the two states in detail.

Cryo-EM structural analysis of NSF in the ADP-AlFx state

The cryo-EM images of NSF in the ADP-AlFx state show features that are consistent with the negative staining images (**Supplementary Fig. 2a**). In total, 22,758 particles were used for the 3D reconstruction, with six-fold symmetry imposed, achieving 9.2-Å resolution at Fourier shell correlation (FSC) = 0.5 (**Fig. 2a** and **Supplementary Fig. 2b**–**e**). We also carried out an independent reconstruction with three-fold symmetry imposed and didn't detect much difference between this reconstruction and the six-fold symmetrized model (**Supplementary Fig. 3a**). Therefore, we focused on the reconstruction with a six-fold symmetry imposed, because it had higher resolution. The reconstruction reveals a 127-Å-tall three-layered barrel-shaped structure (**Fig. 2a**–**c**), which has a shape similar to the reconstruction from the negative stain EM data but shows more detailed features, such as some secondary structure elements. The diameter of D2 is ~112 Å and that of D1 is ~122 Å. The N domain is stacked on the top with lower density and is probably averaged out owing to structural flexibility. The D1 hexamer has a central pore with a uniform diameter of ~20 Å, and the D2 hexamer central pore is tapered from ~24 Å at the top to ~7 Å at the bottom (**Fig. 2c**).

The high-resolution reconstruction allowed us to dock the available crystal structures of the D2 domain (PDB 1NSF) and D1 domain homolog, p97-D1 hexamer (PDB 3HU2, **Supplementary Fig. 4a**,**b**), into the cryo-EM map (**Fig. 2a**). We were already able to carry out rigid-body docking of the two hexameric atomic models into the map quite well. After further flexible fitting of the atomic models, we obtained the final pseudoatomic models of the D2 and D1 domains, with cross-correlation coefficients at 0.92 and 0.89, respectively, to the cryo-EM density (**Fig. 2d**,**e**, **Supplementary Movie 1** and **Supplementary Table 1**), validating the accuracy of our reconstruction. The flexibly fitted models changed very little compared to the original structure models used for the rigid-body docking, with r.m.s. deviations of 3.1 Å and 2.8 Å, respectively, for the D2 and D1 domains. Secondary structural elements such as helix α3 in the D2 domain[17] and helices α3, α4, α1′ and α8′ in the D1 domain are clearly resolved in the map (**Fig. 2f**–**i**). The fitting results also revealed that compared to the D2 domain, the D1 domain shows a more open conformation between the C-terminal helical subdomain (small subdomain) and the N-terminal nucleotide-binding subdomain (large subdomain), resulting in an expanded ring in the D1 hexamer.

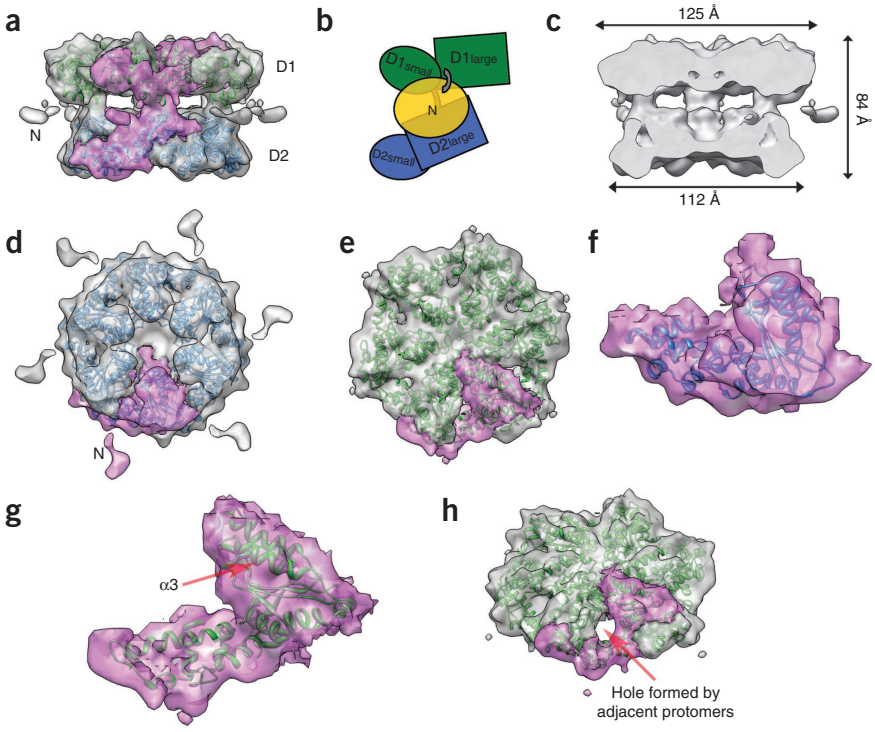

Figure 3 Cryo-EM structure of NSF in the ADP state. (**a**) The 3D reconstruction of NSF in the ADP state at 10-Å resolution with the crystal structure docked (D2 in blue, D1 in green). The D2 hexamer crystal structure and the D1 structure modeled from the p97 D1 hexamer crystal structure were used for flexible fitting in all the structures shown. One protomer is highlighted in purple. The orientation shown is the same as in the ADP-AlFx state depicted in **Figure 2a**. (**b**) A schematic presentation of a protomer in NSF hexamer in ADP state showing the relationship of the large and small subdomains within D1 and D2. (**c**) Cut-open side view of the 3D reconstruction of NSF in the ADP state. (**d**,**e**) Top views of the D2 and D1 hexamer maps isolated from the 3D reconstruction of NSF as shown in **a**. One protomer is highlighted in purple. (**f**,**g**) Zoomed-in top views of D2 and D1 protomers isolated from **d** and **e**, respectively. Helix α3 in D1 is indicated by the red arrow. (**h**) A 45° tilted view of the D1 hexamer map shown in **e**. The hole formed by adjacent protomers is indicated by the red arrow.

The linkers between the D1 and D2 domains are resolved unambiguously (**Fig. 2a**), whereas those between the N and D1 domains are barely visible at a lower density threshold because of their flexibility (**Supplementary Fig. 2f**). By comparison, the N-D1 linkers are more visible in the reconstruction of the 20S particle (see below). The docking analysis and the localization of D1-D2 and N-D1 linkers imply a possible topology of the NSF protomer in the 3D map, which has a three-stepped spiral shape, with the D2 domain at the bottom, the D1 domain in the middle and the N domain at the top (**Fig. 2a**,**b**). The D2 and D1 domains are organized in a parallel, head-to-tail manner (**Supplementary Fig. 2g**), with D1 rotating anticlockwise for ~20° relative to the D2 domain around the symmetry axis. This parallel arrangement of the D1 and D2 domains of hexameric NSF contradicts that reported previously, which was based on a cryo-EM structure[24], but it is consistent with the topology from the crystal structure of p97 (refs. 25,26).

Cryo-EM structural analysis of NSF in the ADP state

The cryo-EM structure of NSF in the ADP state was reconstructed from 34,735 particles with six-fold symmetry imposed, achieving a resolution of 10 Å, estimated at FSC = 0.5 (**Supplementary Fig. 5a–e**; for comparison, the three-fold symmetrized model is shown in **Supplementary Fig. 3b**). The map shows a two-layered barrel structure with a height of ~84 Å. The diameter of D2 is ~112 Å

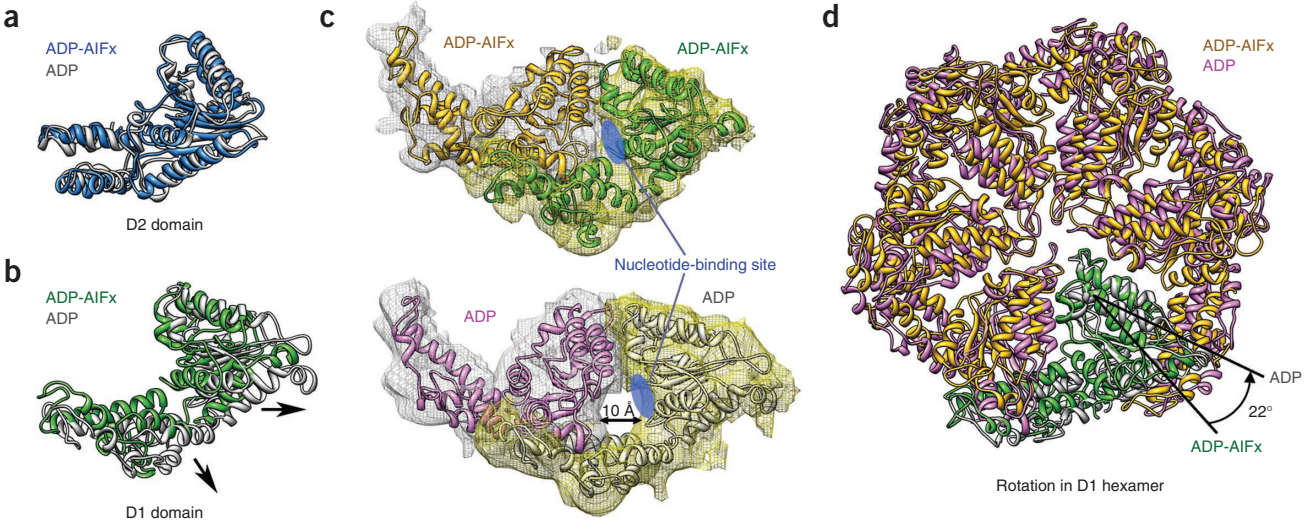

Figure 4 Comparison of D2 and D1 structures in the ADP-AlFx and ADP states. (**a**) The D2 domains in the ADP-AlFx and ADP states were merged for comparison. (**b**) The D1 domains in the ADP-AlFx and ADP states were merged with SUPERPOSED for comparison. From the ADP-AlFx to the ADP state, the nucleotide-binding subdomain and C-terminal helical subdomain move in different directions, as indicated by the arrows. (**c**) Two adjacent D1 protomers in the ADP-AlFx and ADP states are shown with corresponding cryo-EM density maps in mesh. A hole of ~10 Å in diameter exists between the two adjacent protomers in the ADP state. (**d**) Anticlockwise rotation (view from the top) of the D1 hexamer from the ADP-AlFx state to the ADP state.

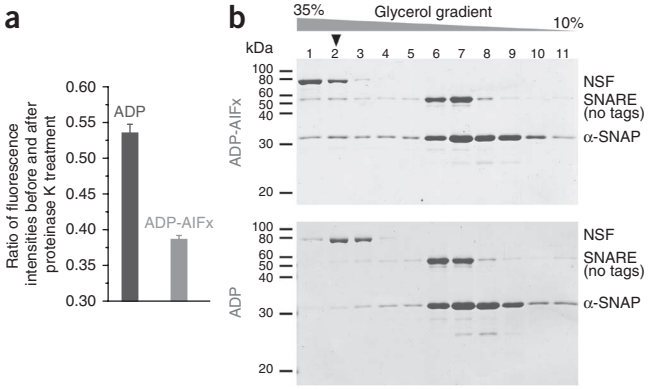

Figure 5 Biochemical analyses of N domain movement and substrate binding activity. (**a**) Comparison of fluorescence emission intensities of the NSF hexamer in the ADP and ADP-AlFx states before and after digestion with proteinase K. The N-terminal His_6-tag of NSF was labeled with nickel–nitrilotriacetic acid fluorescein isothiocyanate. Excitation: 494 nm. Emission: 521 nm. Measurements were repeated three times ($P < 0.0001$). Error bars, s.d. (**b**) Glycerol gradient centrifugation experiment to test the α-SNAP–SNARE binding activity of NSF in the ADP-AlFx and ADP states. Samples were analyzed by SDS-PAGE without boiling and gels were stained with Coomassie blue.

and that of D1 is ~125 Å (**Fig. 3a–c**). The densities of six N domains are splayed around the side of the barrel and do not show any apparent connection with the barrel, suggesting that their flexibility is high (**Figs. 1f,g** and **3a–c**). Connections between the N and D1 domains could be seen when the map was low-pass filtered (**Supplementary Fig. 5f,g**).

We also carried out flexible docking of the available crystal structures into the cryo-EM map of the ADP state by applying the same approach that we used for the ADP-AlFx state. However, in contrast to the ADP-AlFx state, in order to generate a good fit of the atomic models in NSF, the ADP state required a large change of the atomic model to be introduced in the D1 domain docking (with an r.m.s. deviation of 5.4 Å between the docked model and the original structure model). The nucleotide-binding subdomain and the helical subdomain are well determined in both the D2 and D1 domains (**Fig. 3d–g** and **Supplementary Movie 2**). Helix α3 in the D1 domain fits well to the protrusion density in the map (**Fig. 3g**). The major structural features of the D1 domain in the ADP state that differ from the ADP-AlFx state are the large holes between adjacent protomers (**Fig. 3h**) as well as the disappearance of the central pore in the D1 hexamer (**Fig. 3c**), which is probably due to the movement of the pore loops. These findings imply that large conformational changes occur during state transition.

Structural comparison between the ADP-AlFx and ADP states

To compare the structures of NSF in the two nucleotide states, we aligned the two cryo-EM 3D maps at their D2 hexameric ring, which has little ATPase activity and is considered rigid. The D2 domains between the two states are very similar in both the cryo-EM map and the docked atomic models (the r.m.s. deviation between the two models in **Fig. 4a** is 2.5 Å). By contrast, a marked conformational difference is observed in the D1 domain. In the ADP state, the nucleotide-binding subdomain and C-terminal helical subdomain move outward in orthogonal directions (**Fig. 4b**). The C-terminal helical subdomain rotates by ~15° relative to the nucleotide-binding subdomain (**Supplementary Fig. 6**). The movement between the two subdomains of the D1 domain results in a hole with a diameter of ~10 Å near the nucleotide binding site between the adjacent protomers (**Fig. 4c**)[28]. This hole separates the residues contributing to nucleotide binding in helix α8 of the helical subdomain from the nucleotide binding pocket, causing a more exposed nucleotide binding site for the exchange of free nucleotides. Moreover, this movement of the helical subdomain with respect to the nucleotide-binding subdomain, upon ATP hydrolysis, leads to an anticlockwise rotation (view from the top) of the D1 hexameric ring relative to the stable platform of D2 around the symmetric axis in a restricted angular range (22° in helix α3) (**Fig. 4d** and **Supplementary Movie 3**), providing a possible mechanism for converting chemical energy from ATP hydrolysis into mechanical work.

Biochemical analyses of conformational changes in NSF

The nucleotide dependence of N domain translocation within an NSF hexamer was further characterized by fluorescence quenching analysis. The N-terminal His_6-tag of NSF was labeled with nickel–nitrilotriacetic acid fluorescein isothiocyanate (see **Supplementary Methods**). The change in the crowding of the N domains of NSF in response to the nucleotide state was measured by the self-quenching of fluorescence emission, in which more crowded fluorescence dyes

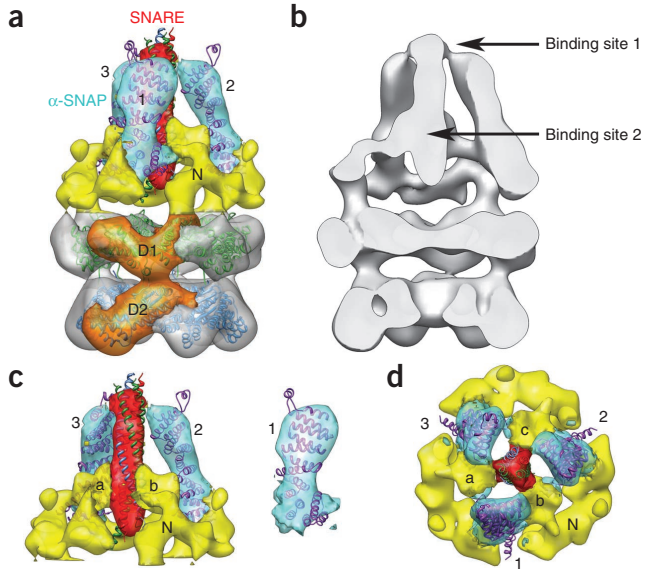

Figure 6 The 3D reconstruction of 20S particles. (**a**) Side view of the 3D reconstruction of the 20S particle built by negative stain EM with c3 symmetry imposed. The cryo-EM structures of D2 (blue) and D1 (green) in the ADP-AlFx state (**Fig. 2a**) were docked onto the map. One protomer in each of the D2 and D1 domains is highlighted in gold. The SNARE complex crystal structure (PDB 1SFC) was docked onto the map (colored in red) (see Online Methods). The crystal structure of the α-SNAP homolog protein in yeast, sec17 (PDB 1QQE), was docked (see Online Methods) onto the densities labeled 1, 2 and 3 (colored in light blue). The densities not overlaid by any crystal structure (colored in yellow) are contributed by the N domain of NSF. (**b**) Cut-open side view of the 20S particle structure with c3 symmetry imposed. The two sites where the SNARE complex is held in the 20S particle are indicated by arrows. (**c**) Interactions between the SNARE complex, α-SNAPs and NSF-N are shown. EM densities corresponding to NSF-D1 and NSF-D2 were cut away from **a**. The density corresponding to α-SNAP-1 was removed and is shown separately on the right. (**d**) Top view of 20S particle structure with NSF-D1 and NSF-D2 cut away. Densities of the NSF-N in close proximity to the N terminal region of the SNARE complex are labeled a, b, and c.

resulted in higher quenching efficiency. Fluorescence emission was quenched more significantly in the presence of ADP-AlFx than in the presence of ADP (**Fig. 5a**), which is consistent with our EM observations that the N domains of NSF in the up conformation of the ADP-AlFx state gathered closer together than those in the down conformation of the ADP state.

A prediction of the hydrodynamic properties of NSF, based on our EM structures using HYDROPRO[29], indicated that NSF in the ADP-AlFx state should have a higher sedimentation coefficient than it does in the ADP state (**Supplementary Table 2**). This prediction agrees with a recent report, which indicated that NSF in its AMP-PNP–bound form sedimented more rapidly than in the ADP-bound form[30], because AMP-PNP and ATPγS are both analogs to ATP, and NSF has similar EM structures in the ATPγS and ADP-AlFx states. Moveover, the down conformation of NSF (in the ADP state) was accompanied by a markedly reduced α-SNAP–SNARE complex substrate binding affinity, as revealed by our glycerol gradient centrifugation results (**Fig. 5b**). The SNARE complex and α-SNAP migrated with NSF in the ADP-AlFx state, forming 20S particles. By contrast, little comigration of the substrates was detected with NSF in the ADP state.

Architecture of the 20S particle

Based on the results of the substrate binding assays, we prepared monodispersed 20S particles by incubating NSF in the ADP-AlFx state with excess SNARE complex and α-SNAP and then separating the assembled complex by glycerol gradient centrifugation (**Fig. 5b** and **Supplementary Fig. 7**). Several populations of particles were found in the negative stain EM images: spark plug–shaped 20S particles, aggregates of multiple 20S particles, and NSF particles (**Supplementary Fig. 8a**). The aggregates were excluded by particle picking. The NSF particles were distinguished by classification, or by classifying all the particles during data processing according to the obvious differences in appearance between the NSF and 20S complexes in both the side and top views. The 3D reconstruction of the 20S particle was obtained from 32,855 particles by projection-matching refinement against an initial model generated from the negative stain EM map of NSF in the ADP-AlFx state, with the density of the N domain portion removed.

Because the top-view class averages of 20S particles show a three-fold rather than a six-fold symmetry of the NSF, three-fold (c3 model) and six-fold (c6 model) symmetries were tested independently for the 3D reconstruction (**Supplementary Figs. 8b–e** and **9**). The models imposed with the two different symmetries have similar overall shapes. Between the two models, the D2 and D1 domains are the same as those seen in NSF. Above the D1 domain, the difference between the c3 and c6 models becomes obvious (**Supplementary Fig. 9b**), especially in cross-sections 1–3, where α-SNAPs are believed to be located[23]. The crystal structure of the α-SNAP homolog sec17 fits better into the c3 model than the c6 model (see below), implying that three copies of α-SNAP bind to one SNARE complex. This analysis is also consistent with our cross-linking data (**Supplementary Fig. 8f**) and with previous biochemical results[31,32]. Therefore, we used the c3 model for further analysis and the c6 model to guide the localization of different structural components in the reconstruction.

The 20S particle shows a spark plug–shaped structure (**Fig. 6a**,**b**). The hexameric rings of the D2 and D1 domains are in conformations similar to those observed in the free NSF. Above the D1 domain, there is a rod-like density in the center that has a similar shape to the SNARE complex. Indeed, the crystal structure of the SNARE complex (PDB 1SFC)[4] can be docked well into the rod-like density (**Fig. 6c**,**d**), with its N terminus facing the D1 domain of NSF. The orientation of the SNARE complex in the 20S particle was previously reported[23]. We verified this orientation by examining 20S particles comprising the SNARE complex with a maltose binding protein tag at the C terminus of the VAMP protein (**Supplementary Fig. 10**). Three copies of the crystal structure of sec17 (PDB 1QQE)[27], an α-SNAP homolog in yeast, were then docked (see Online Methods). The N-terminal region of α-SNAP, which has a typical sheet structure formed by anti-parallel helices, fit well into the EM map (**Fig. 6c**). The N-terminal loop of α-SNAP, which has been proposed as a membrane attachment site[33], is located at the C terminus of the SNARE complex, near its transmembrane domain. The docking results revealed that the N termini of three α-SNAPs contact the C-terminal region of the SNARE complex directly, forming a tripod structure. The electropositive concave faces of the α-SNAPs interact with the electronegative surface of the SNARE complex, in agreement with mutagenesis studies[34] (**Supplementary Fig. 8g**).

The pseudoatomic models of D1 and D2 obtained from the cryo-EM structure of NSF in the ADP-AlFx state can be fitted accurately into the EM map of the 20S particle, indicating a fairly rigid structure of the D1 and D2 domain upon substrate recruitment at the current resolution. On the other hand, although the linker region between the D1 and the N domains was recognizable, the kidney-shaped crystal structure of the N domain[19,20] could not be fitted properly into the EM map. This may be due to the symmetrical inconsistency at the N domain–substrate interface during the reconstruction or to the flexibility of the N domains. The N domain of NSF in the 20S particle is in the up conformation, which is consistent with observations from free NSF in the ADP-AlFx state, implying that the up conformation is a ready state for substrate binding. Each α-SNAP has two contact regions between its C terminus and the N domains of adjacent NSF protomers, forming a support for the legs of the tripod structure. This finding is supported by previous biochemical analyses demonstrating that the monomeric N domain is incapable of binding to the SNAP–SNARE complex[16]. From our structure, we can see that NSF's N domains are in close proximity to the N-terminal region of the SNARE complex (**Fig. 6d**). The SNARE complex is probably positioned in the 20S particle by anchors at both ends: one around the C-terminal region of the SNARE complex where it is fixed by three α-SNAPs and the other in its N-terminal half, where it is anchored by NSF's N domains.

DISCUSSION

In the present work, we reconstructed 3D structures of NSF in its functional cycle: NSF in the ATP state (ATPγS and ADP-AlFx states in our experiments), which is capable of binding substrates; the 20S particle, consisting of the NSF hexamer, three α-SNAPs and the SNARE complex; and NSF in the ADP state (**Supplementary Fig. 11**). These structures revealed that the two AAA+ domains of NSF, D1 and D2, are in a parallel arrangement in the full-length NSF hexamer, similarly to p97, as shown in its full-length hexamer crystal structures[25,26,35].

Our cryo-EM reconstructions of NSF showed that the N domains are flexible, consistent with previous cryo-EM studies of NSF[24] and p97 (ref. 36). The motion mechanics of the p97-N domain is still being debated, owing to varying results from different samples[25,26,35–42]. Cryo-EM reconstruction of p97 in the ADP-AlFx state[36] and crystal structures of p97 in various nucleotide states[25,26,35] previously showed that p97-N was located at the periphery in the same plane with p97-D1. However, in cryo-EM studies of p97 in the AMP-PNP state[39] and p97–p47 complex[41], and in a recent crystal structure of IBMPFD mutants of the p97 N-D1 fragment in the ATP state[43], the p97-N was located above the p97-D1 plane. One important finding of our present work is that we have clearly characterized the nucleotide-dependent up-to-down

movement of NSF-N in the full-length NSF hexamer, namely, NSF-N is in an up conformation in the ATP state and in a down conformation in the ADP state (**Fig. 1g**). Moreover, our 20S particle structure shows that NSF-N is in an up conformation after binding to α-SNAPs and to the SNARE complex in the ADP-AlFx state. Together with substrate binding activity assays, our structures suggest that the up conformation of NSF-N may be a ready state for substrate binding.

Previous cryo-EM studies of p97 in different nucleotide states suggested that the D1 and D2 rings rotated with respect to each other[36]. In our cryo-EM structures of NSF, we found that NSF-D1 rotated anticlockwise relative to NSF-D2 after γ-phosphate release (view from the top of D1). Our docking analysis further revealed that the rotation was caused by the relative movement between the large subdomain and small subdomain within an NSF-D1 protomer through ATP hydrolysis (**Supplementary Fig. 6**). Thus, our NSF studies and previous p97 studies both suggest a possible mechanism for converting the energy from ATP hydrolysis into mechanical movement. Although the similarity between NSF and p97 is obvious, there are substantial differences between the two proteins. In NSF, the D1 domain is mainly responsible for its ATPase activity, whereas in p97, the D2 domain is the major ATPase[44]. The transfer of rotation from NSF-D1 to NSF-N thus spans only a short intramolecular distance compared to that from p97-D2 to p97-N[36]. Various data suggest that binding of NSF to its adaptor protein α-SNAP requires the presence of the SNARE complex[32] (**Supplementary Fig. 7**) and also requires that NSF is in the ATP state rather than in the ADP state[22] (**Fig. 5b**). However, p97 can form a stable complex with its adaptor protein p47 alone, both in the ATP state and the ADP state[37,41].

AAA+ ATPases involved in protein degradation and disaggregation, such as ClpX[45], ClpA[46], ClpB, Hsp104 (ref. 47) and the 26S proteasome[48], handle substrates by threading them through the central pore. However, this mechanism is not applicable to NSF[11,49]. To disassemble the stable SNARE complex, a force must be generated to separate the complex into individual proteins. The anticlockwise rotation of NSF-D1 upon ATP hydrolysis and γ-phosphate release would be coupled to the SNARE complex through the interaction between the N-domain and the α-SNAP–SNARE complex. The up-to-down movement of the NSF-N after γ-phosphate release, which may be coupled to the rotation of the NSF-D1 by an N-D1 linker such as p97 (**Supplementary Fig. 4c**)[43], may support NSF functioning by (i) serving as a substrate recognition mechanism, (ii) releasing the substrate after its disassembly, to avoid reassembly, and (iii) providing a force to disassemble the SNARE complex. Our structural analyses described here may serve as a guide for further studies of the mechanism underlying the SNARE complex disassembly. The conformational changes detected in NSF may also be applicable to other AAA+ proteins that use ATP hydrolysis to disassemble protein complexes.

METHODS

Methods and any associated references are available in the online version of the paper at http://www.nature.com/nsmb/.

Accession codes. The cryo-EM density maps of NSF in the ADP-AlFx and ADP states were deposited in the Electron Microscopy Data Bank with the accession codes EMD-5370 and EMD-5371.

Note: Supplementary information is available on the Nature Structural & Molecular Biology website.

ACKNOWLEDGMENTS

We are grateful to E.R. Chapman (University of Wisconsin, Madison), J. Rizo (University of Texas Southwestern Medical Center) for providing plasmids. We thank F. Zhang, N. Gao, J.-W. Wu, N. Yan, J. Wang and L. Cheng for helpful discussions. We also thank J. Lei for setting up a semiautomated data collection program and Y. Wu for providing electron microscope for our use at the early stage of this work. This work was supported by the National Basic Research Program of China (2011CB910500/2010CB833706/2010CB912400) and the National Natural Science Foundation of China (30830028).

AUTHOR CONTRIBUTIONS

L.-F.C., S.C. and C.-C.L. conducted the experiments and analyzed the data with the help of X.P., J.J., X.-C.B. and X.X.; L.-F.C. prepared the figures; H.-W.W. commented on the experiments; J.J. and H.-W.W edited the manuscript; L.-F.C., S.C. and S.-F.S. planned the experiments and prepared the manuscript; S.-F.S. coordinated the project.

COMPETING FINANCIAL INTERESTS

The authors declare no competing financial interests.

Published online at http://www.nature.com/nsmb/.
Reprints and permissions information is available online at http://www.nature.com/reprints/index.html.

1. Rothman, J.E. Mechanisms of intracellular protein transport. *Nature* **372**, 55–63 (1994).
2. Jahn, R. & Scheller, R.H. SNAREs—engines for membrane fusion. *Nat. Rev. Mol. Cell Biol.* **7**, 631–643 (2006).
3. Söllner, T. *et al.* SNAP receptors implicated in vesicle targeting and fusion. *Nature* **362**, 318–324 (1993).
4. Sutton, R.B., Fasshauer, D., Jahn, R. & Brunger, A.T. Crystal structure of a SNARE complex involved in synaptic exocytosis at 2.4 Å resolution. *Nature* **395**, 347–353 (1998).
5. Stein, A., Weber, G., Wahl, M.C. & Jahn, R. Helical extension of the neuronal SNARE complex into the membrane. *Nature* **460**, 525–528 (2009).
6. Antonin, W., Fasshauer, D., Becker, S., Jahn, R. & Schneider, T.R. Crystal structure of the endosomal SNARE complex reveals common structural principles of all SNAREs. *Nat. Struct. Biol.* **9**, 107–111 (2002).
7. Weber, T. *et al.* SNAREpins: minimal machinery for membrane fusion. *Cell* **92**, 759–772 (1998).
8. Söllner, T., Bennett, M.K., Whiteheart, S.W., Scheller, R.H. & Rothman, J.E. A protein assembly-disassembly pathway *in vitro* that may correspond to sequential steps of synaptic vesicle docking, activation, and fusion. *Cell* **75**, 409–418 (1993).
9. Mayer, A., Wickner, W. & Haas, A. Sec18p (NSF)-driven release of Sec17p (alpha-SNAP) can precede docking and fusion of yeast vacuoles. *Cell* **85**, 83–94 (1996).
10. Wilson, D.W., Whiteheart, S.W., Wiedmann, M., Brunner, M. & Rothman, J.E. A multisubunit particle implicated in membrane fusion. *J. Cell Biol.* **117**, 531–538 (1992).
11. Hanson, P.I. & Whiteheart, S.W. AAA+ proteins: have engine, will work. *Nat. Rev. Mol. Cell Biol.* **6**, 519–529 (2005).
12. Ogura, T. & Wilkinson, A.J. AAA+ superfamily ATPases: common structure–diverse function. *Genes Cells* **6**, 575–597 (2001).
13. Fleming, K.G. *et al.* A revised model for the oligomeric state of the N-ethylmaleimide-sensitive fusion protein, NSF. *J. Biol. Chem.* **273**, 15675–15681 (1998).
14. Tagaya, M., Wilson, D.W., Brunner, M., Arango, N. & Rothman, J.E. Domain structure of an N-ethylmaleimide-sensitive fusion protein involved in vesicular transport. *J. Biol. Chem.* **268**, 2662–2666 (1993).
15. Zhao, C., Smith, E.C. & Whiteheart, S.W. Requirements for the catalytic cycle of the N-ethylmaleimide-sensitive factor (NSF). *Biochim. Biophys. Acta* **1823**, 159–171 (2012).
16. Nagiec, E.E., Bernstein, A. & Whiteheart, S.W. Each domain of the N-ethylmaleimide-sensitive fusion protein contributes to its transport activity. *J. Biol. Chem.* **270**, 29182–29188 (1995).
17. Lenzen, C.U., Steinmann, D., Whiteheart, S.W. & Weis, W.I. Crystal structure of the hexamerization domain of N-ethylmaleimide-sensitive fusion protein. *Cell* **94**, 525–536 (1998).
18. Yu, R.C., Hanson, P.I., Jahn, R. & Brunger, A.T. Structure of the ATP-dependent oligomerization domain of N-ethylmaleimide sensitive factor complexed with ATP. *Nat. Struct. Biol.* **5**, 803–811 (1998).
19. May, A.P., Misura, K.M., Whiteheart, S.W. & Weis, W.I. Crystal structure of the amino-terminal domain of N-ethylmaleimide-sensitive fusion protein. *Nat. Cell Biol.* **1**, 175–182 (1999).
20. Yu, R.C., Jahn, R. & Brunger, A.T. NSF N-terminal domain crystal structure: models of NSF function. *Mol. Cell* **4**, 97–107 (1999).
21. Babor, S.M. & Fass, D. Crystal structure of the Sec18p N-terminal domain. *Proc. Natl. Acad. Sci. USA* **96**, 14759–14764 (1999).
22. Hanson, P.I., Roth, R., Morisaki, H., Jahn, R. & Heuser, J.E. Structure and conformational changes in NSF and its membrane receptor complexes visualized by quick-freeze/deep-etch electron microscopy. *Cell* **90**, 523–535 (1997).
23. Hohl, T.M. *et al.* Arrangement of subunits in 20S particles consisting of NSF, SNAPs, and SNARE complexes. *Mol. Cell* **2**, 539–548 (1998).

24. Furst, J., Sutton, R.B., Chen, J., Brunger, A.T. & Grigorieff, N. Electron cryomicroscopy structure of N-ethyl maleimide sensitive factor at 11 Å resolution. *EMBO J.* **22**, 4365–4374 (2003).
25. DeLaBarre, B. & Brunger, A.T. Complete structure of p97/valosin-containing protein reveals communication between nucleotide domains. *Nat. Struct. Biol.* **10**, 856–863 (2003).
26. Huyton, T. *et al.* The crystal structure of murine p97/VCP at 3.6 Å. *J. Struct. Biol.* **144**, 337–348 (2003).
27. Rice, L.M. & Brunger, A.T. Crystal structure of the vesicular transport protein Sec17: implications for SNAP function in SNARE complex disassembly. *Mol. Cell* **4**, 85–95 (1999).
28. Suno, R. *et al.* Structure of the whole cytosolic region of ATP-dependent protease FtsH. *Mol. Cell* **22**, 575–585 (2006).
29. Ortega, A., Amoros, D. & Garcia de la Torre, J. Prediction of hydrodynamic and other solution properties of rigid proteins from atomic- and residue-level models. *Biophys. J.* **101**, 892–898 (2011).
30. Zhao, C. *et al.* Hexahistidine-tag-specific optical probes for analyses of proteins and their interactions. *Anal. Biochem.* **399**, 237–245 (2010).
31. Rossi, G., Salminen, A., Rice, L.M., Brunger, A.T. & Brennwald, P. Analysis of a yeast SNARE complex reveals remarkable similarity to the neuronal SNARE complex and a novel function for the C terminus of the SNAP-25 homolog, Sec9. *J. Biol. Chem.* **272**, 16610–16617 (1997).
32. Wimmer, C. *et al.* Molecular mass, stoichiometry, and assembly of 20S particles. *J. Biol. Chem.* **276**, 29091–29097 (2001).
33. Winter, U., Chen, X. & Fasshauer, D. A conserved membrane attachment site in alpha-SNAP facilitates N-ethylmaleimide-sensitive factor (NSF)-driven SNARE complex disassembly. *J. Biol. Chem.* **284**, 31817–31826 (2009).
34. Marz, K.E., Lauer, J.M. & Hanson, P.I. Defining the SNARE complex binding surface of alpha-SNAP: implications for SNARE complex disassembly. *J. Biol. Chem.* **278**, 27000–27008 (2003).
35. Davies, J.M., Brunger, A.T. & Weis, W.I. Improved structures of full-length p97, an AAA ATPase: implications for mechanisms of nucleotide-dependent conformational change. *Structure* **16**, 715–726 (2008).
36. Rouiller, I. *et al.* Conformational changes of the multifunction p97 p97 AAA ATPase during its ATPase cycle. *Nat. Struct. Biol.* **9**, 950–957 (2002).
37. Rouiller, I., Butel, V.M., Latterich, M., Milligan, R.A. & Wilson-Kubalek, E.M. A major conformational change in p97 AAA ATPase upon ATP binding. *Mol. Cell* **6**, 1485–1490 (2000).
38. Rockel, B., Jakana, J., Chiu, W. & Baumeister, W. Electron cryo-microscopy of VAT, the archaeal p97/CDC48 homologue from *Thermoplasma acidophilum*. *J. Mol. Biol.* **317**, 673–681 (2002).
39. Beuron, F. *et al.* Motions and negative cooperativity between p97 domains revealed by cryo-electron microscopy and quantised elastic deformational model. *J. Mol. Biol.* **327**, 619–629 (2003).
40. Davies, J.M., Tsuruta, H., May, A.P. & Weis, W.I. Conformational changes of p97 during nucleotide hydrolysis determined by small-angle X-Ray scattering. *Structure* **13**, 183–195 (2005).
41. Beuron, F. *et al.* Conformational changes in the AAA ATPase p97-p47 adaptor complex. *EMBO J.* **25**, 1967–1976 (2006).
42. Pye, V.E. *et al.* Going through the motions: the ATPase cycle of p97. *J. Struct. Biol.* **156**, 12–28 (2006).
43. Tang, W.K. *et al.* A novel ATP-dependent conformation in p97 N-D1 fragment revealed by crystal structures of disease-related mutants. *EMBO J.* **29**, 2217–2229 (2010).
44. Brunger, A.T. & DeLaBarre, B. NSF and p97/VCP: similar at first, different at last. *FEBS Lett.* **555**, 126–133 (2003).
45. Baker, T.A. & Sauer, R.T. ClpXP, an ATP-powered unfolding and protein-degradation machine. *Biochim. Biophys. Acta* **1823**, 15–28 (2012).
46. Effantin, G., Ishikawa, T., De Donatis, G.M., Maurizi, M.R. & Steven, A.C. Local and global mobility in the ClpA AAA+ chaperone detected by cryo-electron microscopy: functional connotations. *Structure* **18**, 553–562 (2010).
47. Lee, S., Sielaff, B., Lee, J. & Tsai, F.T. CryoEM structure of Hsp104 and its mechanistic implication for protein disaggregation. *Proc. Natl. Acad. Sci. USA* **107**, 8135–8140 (2010).
48. Bohn, S. *et al.* Structure of the 26S proteasome from *Schizosaccharomyces pombe* at subnanometer resolution. *Proc. Natl. Acad. Sci. USA* **107**, 20992–20997 (2010).
49. May, A.P., Whiteheart, S.W. & Weis, W.I. Unraveling the mechanism of the vesicle transport ATPase NSF, the N-ethylmaleimide-sensitive factor. *J. Biol. Chem.* **276**, 21991–21994 (2001).

ONLINE METHODS

Protein expression and purification. Plasmids encoding $VAMP_{1–94}$, $SNAP\text{-}25_{1–100}$, $SNAP\text{-}25_{125–206}$, NSF and α-SNAP were gifts from E. R. Chapman. The plasmid encoding $Syntaxin_{2–253}$ was provided by J. Rizo. All plasmids were confirmed by DNA sequencing (**Supplementary Fig. 1a**). All proteins were expressed in *Escherichia coli* BL21 (DE3) and purified as His_6-tagged or GST-fused recombinant proteins, using standard procedures. Details appear in the **Supplementary Methods**.

Negative staining and image processing. Freshly purified NSF (4 μL, 10 μg ml^{-1}) in different nucleotide states or 20S particles (10 μg ml^{-1}) that were immediately separated from glycerol gradient centrifugation were applied to glow-discharged EM grids with continuous carbon. After 30 s, excess sample was blotted, and the grid was washed twice with 2% (w/v) uranyl acetate and stained for 30 s. Samples were dried and transferred into a Tecnai F20 electron microscope (FEI) operated at 200 kV. Images were recorded with a Gatan 4k × 4k CCD camera at a nominal magnification of 50,000×, yielding a pixel size of 2.23 Å at the sample level. Defocuses were set at about −800 nm.

For data analysis, particles were selected automatically using the EMAN[50] program batchboxer and manually screened. The 2D classification was done using the EMAN program refine2d.py. The initial model of NSF in the ADP-AlFx state was determined using the random conical tilt method (details appear in the **Supplementary Methods**), which was used for the refinement of NSF in the three different states (ATPγS, ADP-AlFx and ADP). In total, 21,138 particles were used for NSF reconstruction in the ATPγS state, 24,434 particles for reconstruction in the ADP-AlFx state and 52,367 particles for reconstruction in the ADP state (**Fig. 1f**).

For the reconstruction of 20S particles, ~73,000 particles were selected from 2,160 negative staining micrographs. These particles were classified using refine2d.py. From the 2D averages, particles without α-SNAP–SNARE were extensively removed, with 32,855 particles remaining. NSFs are different from 20S particles, because they have no tail in the side view and have an apparent central pore in the top view (**Fig. 1c** and **Supplementary Fig. 8b**). Negative stain EM reconstruction of NSF in the ADP-AlFx state with the N domain density removed (low-pass filtered to 40 Å) was used as the initial model, and c3 or c6 symmetry was imposed for comparison.

Cryo-EM and image processing. Freshly purified NSF (3 μL, 20 μg ml^{-1}) in the ADP-AlFx state (20 mM HEPES-NaOH, pH 7.2, 50 mM NaCl, 2 mM $MgCl_2$, 2 mM ADP, 2 mM $AlCl_3$, 8 mM NaF) or the ADP state (20 mM HEPES-NaOH, pH 7.2, 50 mM NaCl, 2 mM $MgCl_2$, 2 mM ADP) was applied to glow-discharged 300-mesh R1.2/1.3 Quantifoil holey grids coated with thin continuous carbon. The grid was blotted and frozen in liquid ethane using a Vitrobot (FEI). Samples were transferred to a Tecnai F20 electron microscope operated at 200 kV. Images were recorded on a Gatan 4k × 4k CCD camera at a nominal magnification of 62,000× under low-dose conditions (20 e^- per $Å^2$), yielding a pixel size of 1.8 Å at the sample level. Defocuses were set between −1.5 and −3 μm.

We collected 1,200 micrographs for NSF in the ADP-AlFx state and 1,860 micrographs for NSF in the ADP state. For further processing, 340 ADP-AlFx–state and 802 ADP-state micrographs with visible contrast transfer function rings beyond 0.1 $Å^{-1}$ in their Fourier transforms were selected. All image processing and 3D reconstructions were done using the EMAN software package. Particle selection of cryo-EM samples was similar to that with the negatively stained samples. The contrast transfer function parameters were determined manually with the ctfit program. The 2D classification was done using the refine2d.py program. Eigenimages of classification are shown in **Supplementary Figure 12**. Negative stain EM reconstructions (low-pass filtered to 40 Å) were used as the initial model for the cryo-EM reconstruction. During the reconstruction process, six-fold symmetry was imposed for NSF in two states, and particles that changed their orientation assignment more than 12° were excluded from further rounds of refinement. For comparison, reconstruction with three-fold symmetry was also carried out, with the same initial model and refine parameters, except that the symmetry was changed (**Supplementary Fig. 3**). The model was iteratively refined until no further improvement could be obtained. The final resolution was estimated by Fourier shell correlation with a 0.5 cutoff criterion. Final cryo-EM density maps were low-pass filtered to the indicated resolution (9.2 Å for the ADP-AlFx state and 10 Å for the ADP state), with a B factor of 600 $Å^2$ imposed.

Docking analysis and visualization. For docking analysis of the cryo-EM maps, the crystal structure of the D2 hexamer (PDB 1NSF) was used to dock the D2 domain. For D1 docking, we built a structural model (**Supplementary Fig. 4a,b**) in Modeller[51], using the crystal structure of the p97-D1 hexamer (PDB 3HU2) as a template because of its sequence identity to NSF-D1. Docking analyses were separated into two steps. First, the high-resolution hexamer structures of the D2 and D1 domains were rigidly docked into the density map using the colores program in Situs[52]. Second, the rigid docking was flexibly fitted onto the map by molecular dynamics flexible fitting[53]. Map segmentation and visualization were carried out using Chimera[54].

For docking analyses of the 20S particle, the crystal structure of the SNARE complex (PDB 1SFC) was fitted onto the density map with a UCSF Chimera-based one-local optimization strategy. The crystal structure of the α-SNAP yeast homolog Sec17 (PDB 1QQE) was docked onto the density map using the colores program in Situs. The cryo-EM density map of NSF in the ADP-AlFx state, along with the flexibly fitted structure of the D2 and D1 domains, was fitted into 20S particle using 'fit map in map' in Chimera.

Fluorescence labeling and steady-state fluorescence spectroscopy. Details are described in the **Supplementary Methods**.

50. Ludtke, S.J., Baldwin, P.R. & Chiu, W. EMAN: semiautomated software for high-resolution single-particle reconstructions. *J. Struct. Biol.* **128**, 82–97 (1999).
51. Eswar, N. *et al.* Comparative protein structure modeling using Modeller. *Curr. Protoc. Bioinformatics* **Chapter 5** Unit 5.6 (2006).
52. Wriggers, W. & Birmanns, S. Using situs for flexible and rigid-body fitting of multiresolution single-molecule data. *J. Struct. Biol.* **133**, 193–202 (2001).
53. Trabuco, L.G., Villa, E., Schreiner, E., Harrison, C.B. & Schulten, K. Molecular dynamics flexible fitting: a practical guide to combine cryo-electron microscopy and X-ray crystallography. *Methods* **49**, 174–180 (2009).
54. Pettersen, E.F. *et al.* UCSF Chimera–a visualization system for exploratory research and analysis. *J. Comput. Chem.* **25**, 1605–1612 (2004).

doi:10.1038/nsmb.2237